



Article

Substitution versus Full-Heusler Segregation in TiCoSb

Maryana Asaad ¹, Jim Buckman ² and Jan-Willem G. Bos ^{1,*}

¹ Institute of Chemical Sciences and Centre for Advanced Energy Storage and Recovery, School of Engineering and Physical Sciences, Heriot-Watt University, Edinburgh EH14 4AS, UK; maryana.asaad@manchester.ac.uk

² Institute of Petroleum Engineering, School of Energy, Geoscience, Infrastructure and Society, Heriot-Watt University, Edinburgh EH14 4AS, UK; J.Buckman@hw.ac.uk

* Correspondence: j.w.g.bos@hw.ac.uk; Tel.: +44-0131-451-3107

Received: 18 October 2018; Accepted: 8 November 2018; Published: 12 November 2018

Abstract: Half-Heuslers (HHs) are promising thermoelectric materials with great compositional flexibility. Here, we extend work on the p-type doping of TiCoSb using abundant elements. $\text{Ti}_{0.7}\text{V}_{0.3}\text{Co}_{0.85}\text{Fe}_{0.15}\text{Sb}_{0.7}\text{Sn}_{0.3}$ samples with nominal 17.85 p-type electron count were investigated. Samples prepared using powder metallurgy have negative Seebeck values, $S \leq -120 \mu\text{V K}^{-1}$, while arc-melted compositions are compensated semiconductors with $S = -45$ to $+30 \mu\text{V K}^{-1}$. The difference in thermoelectric response is caused by variations in the degree of segregation of $\text{V}(\text{Co}_{0.6}\text{Fe}_{0.4})_2\text{Sn}$ full-Heusler and Sn phases, which selectively absorb V, Fe, and Sn. The segregated microstructure leads to reduced lattice thermal conductivities, $\kappa_{\text{lat}} = 4.5\text{--}7 \text{ W m}^{-1} \text{ K}^{-1}$ near room temperature. The largest power factor, $S^2/\rho = 0.4 \text{ mW m}^{-1} \text{ K}^{-2}$ and $ZT = 0.06$, is observed for the n-type samples at 800 K. This work extends knowledge regarding suitable p-type dopants for TiCoSb.

Keywords: Half-Heusler; TiCoSb; phase segregation; thermoelectric properties

1. Introduction

Thermoelectric waste heat recovery is a promising technology that may help reduce reliance on fossil fuels and mitigate the impacts of climate change. The large-scale application of thermoelectric generators is limited by the availability of cost-effective n- and p-type materials. In this regard, half-Heuslers (HHs) are promising as they combine good performance, use of abundant elements, good mechanical properties, and thermal stability [1,2]. The efficiency of a thermoelectric material is given by its figure of merit, $ZT = (S^2/\rho\kappa)T$, where S is the Seebeck coefficient, ρ is the electrical resistivity, κ is the sum of the lattice (κ_{lat}) and electronic (κ_{el}) thermal conductivities, and T is the absolute temperature [3]. In general, HHs are characterised by large power factors (S^2/ρ), which enables large amounts of power to be extracted from the generators, but are limited by relatively large κ values, which reduces the overall device efficiency [1,2]. The current best materials are based on XNiSn (n-type) [4–7], XCoSb (p-type) [8,9] ($X = \text{Ti, Zr, Hf}$), and X'FeSb (p-type) [10–12] ($X' = \text{V, Nb, Ta}$), while $\text{Nb}_{0.8\text{--}0.9}\text{CoSb}$ alloys have recently emerged as promising new n-type compositions [13,14].

The XYZ HH crystal structure consists of a face centred cubic lattice of main group atoms (Z), with the more electropositive (X) metal occupying all octahedral sites, and the late transition metal (Y) on half the tetrahedral sites [15]. Complete filling of the vacant tetrahedral sites leads to the formation of a full-Heusler (FH) structure. The space group symmetry of the HH structure is cubic F-43m and increases to Fm-3m for the FH structure.

The aim of this work was to develop a good p-type thermoelectric material based on TiCoSb that avoids the use of expensive Zr and Hf. Compared to TiNiSn (see e.g., [16–25]), TiCoSb has attracted

far less interest and does not support the presence of interstitial Co for samples prepared using powder routes [26]. Previous work from our group showed that co-substitution with V and Sn improved the high-temperature stability of TiCoSb [26]. However, these $Ti_{1-x}V_xCoSb_{1-x}Sn_x$ samples maintained an 18-valence electron count and were n-type conductors. Here, we report on our investigation of the $Ti_{0.7}V_{0.3}Co_{0.85}Fe_{0.15}Sb_{0.7}Sn_{0.3}$ samples, where Fe is substituted on the Co-site to obtain a p-type 17.85 valence electron count. Samples were prepared using both powder metallurgy and arc-melting routes. In both cases, segregation of a FH phase rich in V, Fe, and Sn occurs, which absorbs the V, Fe, and Sn substituents. This leads to compensated semiconducting behaviour for the samples prepared using arc melting, while the degree of segregation of V is lower for the samples prepared from powder metallurgy. Hence, leading to clear n-type behaviour. We note that all three elements of V, Fe, and Sn have good individual solubility in TiCoSb [27–29], while V and Sn can be co-substituted up to ~40% [26]. This work raises the important question if it is the energy penalty associated with p-type substitutions (as suggested by theory [30,31]) or the stability of the FH that drives the poor uptake of V, Fe, and Sn in TiCoSb.

2. Experiment

Polycrystalline $Ti_{0.7}V_{0.3}Co_{0.85}Fe_{0.15}Sb_{0.7}Sn_{0.3}$ samples were prepared on a 2.5-gram scale via powder metallurgy and arc melting. A summary of the prepared samples is given in Tables 1 and 2. Starting materials were metal powders of Ti (325 mesh, 99.99%), V (325 mesh, 99.5%), Co (1.6 micron, 99.8%), Fe (<10 micron, 99.5%), Sb (powdered shots, 99.99%), and Sn (100 mesh, 99.85%). All were purchased from Alfa Aesar (Alfa Aesar, Heysham, UK). Appropriate amounts of the constituent elements were mixed using an agate mortar and pestle, and cold pressed into pellets. For the powder route, these were wrapped in Ta foil and sintered in vacuum sealed quartz tubes at 850 °C for 24 h. Samples were then reground, re-pressed, and sintered for an additional 7 days at 850 °C. Subsequent consolidation through hot pressing was performed at 850 °C for 20 min under 80 MPa. To check reproducibility, one repeat sample was prepared using an identical procedure. These samples are labelled SSR-R1, R2 throughout the manuscript. In the case of the arc-melted samples, two different synthesis routes were used. The samples labelled (AM) R1-R3 were prepared by direct arc melting of all elements, while for sample R4, the transition metals were melted first, and the main group elements were added in a subsequent arc-melting step. The samples were melted and turned over at least twice. Following the arc melting, samples R1, R2, and R4 were sintered for 7 days at 850 °C without intermediate homogenisation, while sample R3 was ground using a pestle and mortar, cold pressed and sintered at 850 °C for 24 h, then homogenised and sintered at 850 °C for a further 7 days. As a final step, the arc-melted samples were powdered using mortar and pestle and hot pressed at 850 °C and 80 MPa for 20 min.

Table 1. Overview of the lattice parameters (a), sample densities, 300 K electrical resistivity (ρ) and Seebeck coefficient (S), maximum power factor (S^2/ρ)_{max}, and 323 K thermal conductivity (κ) for the $Ti_{0.7}V_{0.3}Co_{0.85}Fe_{0.15}Sb_{0.7}Sn_{0.3}$ samples prepared by powder metallurgy.

Sample	a (Å)	Density (g·cm ⁻³)	%Density	FH (%)	Sn (%)	ρ_{300K} (mΩ·cm)	S_{300K} (μV·K ⁻¹)	(S^2/ρ) _{max} (mW·m ⁻¹ ·K ⁻²)	κ_{323K} (W·m ⁻¹ ·K ⁻¹)
R1	5.8724(1)	6.9(1)	92(1)	7.1(1)	1.0(1)	2.8	-60.1	0.38	-
R2	5.8711(1)	7.1(1)	95(1)	8.2(3)	0.2(1)	4.1	-85.3	0.32	4.6

Table 2. Overview of the lattice parameters (a), sample densities, 300 K electrical resistivity (ρ) and Seebeck coefficient (S), maximum power factor (S^2/ρ)_{max}, and 323 K thermal conductivity (κ) for the $Ti_{0.7}V_{0.3}Co_{0.85}Fe_{0.15}Sb_{0.7}Sn_{0.3}$ samples prepared by arc melting.

Sample	a (Å)	Density (g cm ⁻³)	%Density	FH (%)	Sn (%)	ρ_{300K} (mΩ·cm)	S_{300K} (μV·K ⁻¹)	(S^2/ρ) _{max} (mW·m ⁻¹ ·K ⁻²)	κ_{323K} (W·m ⁻¹ ·K ⁻¹)
R1	5.8838(1)	6.8(1)	91(1)	10.3(3)	3.8(2)	4.4	-8.9	0.02	-
R2	5.8835(1)	7.0(1)	93(1)	12.8(2)	2.7(3)	2.7	-21.7	0.02	5.8
R3	5.8796(1)	7.1(1)	95(1)	10.9(1)	2.8(2)	2.1	-25.1	0.08	5.6
R4	5.8838(1)	6.8(1)	91(1)	10.2(2)	2.5(2)	3.2	-8.3	0.01	6.9

Laboratory X-ray powder diffraction (XRD) patterns were collected using a D8 Advance diffractometer (Bruker, Billerica, MA, USA) using monochromatic Cu $K\alpha_1$ radiation for a period of 8 h. Rietveld analysis of the powder diffraction data was carried out using the GSAS and EXPGUI programmes [32,33]. The microstructure and homogeneity of the hot-pressed samples were examined using a Quanta 650 FEG Scanning Electron Microscope (FEI, Eindhoven, The Netherlands). Quantitative analysis of selected areas was performed using the AZtec Large Area Maps software (v. 3.3, Oxford Instruments, Abingdon, Oxford, UK). Prior to SEM-EDX analysis, samples were polished to 0.5 μm roughness with Al_2O_3 polishing paper.

For electrical property measurements, bars were cut from the middle of the hot-pressed disks using a low speed diamond saw. The Seebeck coefficient and electrical resistivity were measured simultaneously using a Linseis LSR-3 instrument (Linseis, Selb, Germany). The thermal diffusivity (α) was measured using a Linseis LFA 1000 Laser Flash instrument (Linseis, Selb, Germany). The densities (d) of the samples was calculated from the mass and dimensions of the hot-pressed pellets. The thermal conductivity, $\kappa = \alpha Cd$, was calculated using the experimental α and d values and heat capacity data (C) from the literature [34]. A porosity correction of $\kappa/\kappa_{dense} = 1 - (4/3)\phi$; $\phi = (100 - \%density)/100$ was applied. The lattice thermal conductivity was calculated using $\kappa_{lat} = \kappa - LT/\rho$; where the Lorenz number, L , was estimated using the procedure outlined in Ref. [35].

3. Results

3.1. X-ray Powder Diffraction

The XRD patterns for all prepared samples are shown in Figure 1. Samples prepared using the powder route are labelled SSR, while the arc-melted samples are labelled AM. Inspection of the diffraction patterns reveals a main HH phase with varying amounts of FH and elemental Sn secondary phases. Rietveld analysis was used to obtain the HH lattice parameter and weight fractions of the three phases apparent from XRD. These are summarized in Tables 1 and 2. There is no significant difference in the lattice parameter of the SSR samples with near identical $a = 5.871(1)$ Å. The lattice parameters for the AM samples (R1-4) are somewhat larger with $a = 5.883(2)$ Å, suggesting a different chemical composition. The fitted amounts of FH phase are 7–8% for the SSR samples and increases to 10–12% for the AM samples. The amount of Sn is also found to have increased for the AM samples, from 0.2–1 wt% to 3–4 wt%. The overall conclusion is therefore that the AM samples are more segregated. The sample densities after hot pressing are $7.0(1)$ g cm^{-3} for all samples (91–95% of theoretical), independent on SSR or AM route, and are therefore largely controlled by the hot-pressing procedure.

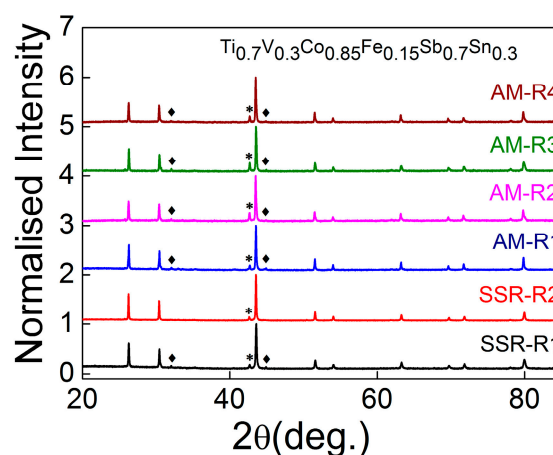


Figure 1. X-ray powder diffraction patterns for the $\text{Ti}_{0.7}\text{V}_{0.3}\text{Co}_{0.85}\text{Fe}_{0.15}\text{Sb}_{0.7}\text{Sn}_{0.3}$ samples prepared using powder metallurgy (SSR) and arc melting (AM). Secondary phases are labelled as *: FH and ◆: Sn.

3.2. Scanning Electron Microscopy

Backscattered electron (BSE) images ($\sim 150 \times 200 \mu\text{m}^2$) and elemental maps for selected SSR (R1) and AM (R4) samples are shown in Figure 2.

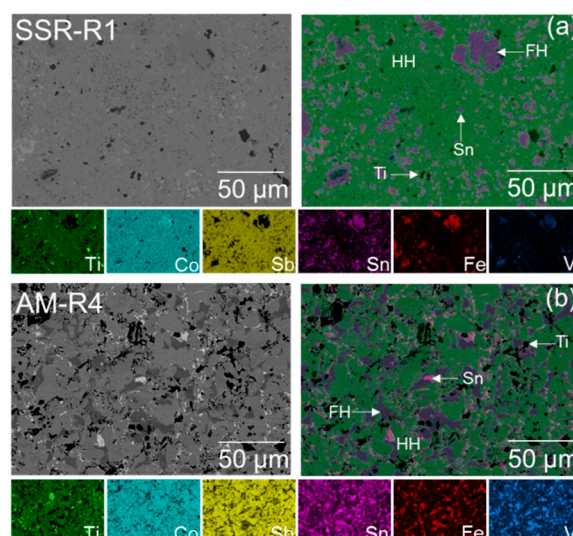


Figure 2. Backscattered scanning electron microscopy images, composite and individual elemental maps for the (a) SSR-R1 and (b) AM-R4 $\text{Ti}_{0.7}\text{V}_{0.3}\text{Co}_{0.85}\text{Fe}_{0.15}\text{Sb}_{0.7}\text{Sn}_{0.3}$ samples. The compositions of the phases present are discussed in the text and are listed in Table 3.

Table 3. SEM-EDX compositions for the half- and full-Heusler (HH and FH) phases present in the $\text{Ti}_{0.7}\text{V}_{0.3}\text{Co}_{0.85}\text{Fe}_{0.15}\text{Sb}_{0.7}\text{Sn}_{0.3}$ samples prepared by powder reactions (SSR) and arc melting (AM). The compositions are the average of >6 equivalent areas taken from different locations on the ingot; the standard deviations reflect the spatial variation in composition. Estimated valence electron counts (VECs) for the HH phases are given.

Sample	SSR (R1)	AM (R4)
HH phase	$\text{Ti}_{0.73(3)}\text{V}_{0.27(3)}\text{Co}_{0.90(2)}\text{Fe}_{0.10(2)}\text{Sb}_{0.88(1)}\text{Sn}_{0.12(1)}$ (VEC = 18.1(8))	$\text{Ti}_{0.92(3)}\text{V}_{0.08(3)}\text{CoSb}_{0.88(1)}\text{Sn}_{0.12(1)}$ (VEC = 18.0(3))
FH phase	$\text{V}(\text{Co}_{0.64(1)}\text{Fe}_{0.36(1)})_2\text{Sn}$	$\text{V}(\text{Co}_{0.59(1)}\text{Fe}_{0.41(1)})_2\text{Sn}$

Brighter areas in the BSE images correspond to regions of a higher average atomic number (Z), while darker areas have a lower average Z . Significant contrast variations are observed in the BSE images, signalling the presence of multiple phases, in agreement with the XRD results. The variations in chemical composition are also evident in the composite and individual EDX elemental maps. There are, however, some clear differences between the SSR and AM samples. The BSE image for the AM sample appears less homogeneous, indicative of a clearer phase segregation, which is in keeping with the XRD results. However, despite the more homogenous appearance of the BSE image for the SSR sample, the elemental maps clearly demonstrate the presence of FH and Sn phases. The FH phases in the SSR sample (purple in the composite maps) have a range of sizes from 1–10 s micron, while elemental Sn (pink) is typically located in smaller areas. There is no obvious correlation between the position of the FH and Sn phases in the SSR samples. By contrast, in the AM sample, the FH and Sn phases tend to appear in close proximity. In addition, the FH regions are more uniformly distributed, while for the SSR sample, fewer, but larger area, FH regions were observed. There are therefore significant differences in microstructure for samples prepared via SSR and AM. Both SSR and AM samples surprisingly also contain some unreacted elemental Ti, as previously observed for TiNiSn [36]. It seems unlikely that this is due to slow reaction kinetics in the case of the AM samples and is more likely to be a consequence of the thermodynamics of this system. The EDX composition of the FH phase is similar in both SSR [$\text{V}(\text{Co}_{0.64(1)}\text{Fe}_{0.36(1)})_2\text{Sn}$] and AM [$\text{V}(\text{Co}_{0.59(1)}\text{Fe}_{0.41(1)})_2\text{Sn}$] samples, where

an average of at least six equivalent regions across the ingot was used in each case. The HH phase makes up most of the samples. The EDX elemental compositions is found to be $\text{Ti}_{0.73(3)}\text{V}_{0.27(3)}\text{Co}_{0.90(2)}\text{Fe}_{0.10(2)}\text{Sb}_{0.88(1)}\text{Sn}_{0.12(1)}$ for the SSR sample, which therefore has a reduced Fe and Sn content compared to nominal. The composition for the AM sample is: $\text{Ti}_{0.92(3)}\text{V}_{0.08(3)}\text{CoSb}_{0.88(1)}\text{Sn}_{0.12(1)}$; i.e., without any Fe on the Co site, a comparable Sn content to the SSR sample and a far lower V content. The approximate valence electron counts for these HH phases are 18.1(8) (SSR) and 18.0(3) (AM), which is at the boundary between n- and p-type conduction. From this analysis, the FH phase forms a sink for the V, Fe, and Sn substituents. The arc melting facilitates a more complete segregation of V and Fe, while the Sn content in the SSR and AM samples is similar. The lower-temperature reaction route enables the SSR sample to retain a larger amount of V, while both Fe and Sn are reduced. The net impact is that most of the electron doping (through V) is maintained, but the compensating p-type doping is reduced. For the AM samples, the V content is much lower and approximately compensated by the p-type carriers from Sn, which is consistent with the observed thermoelectric properties.

3.3. Electrical Properties

The temperature dependences of the electrical resistivity (ρ), Seebeck coefficient (S), and power factor (S^2/ρ) for the SSR and AM samples are given in Figure 3. The SSR samples are n-type with $S_{300\text{K}} = -60 \mu\text{V}\cdot\text{K}^{-1}$ and $S_{300\text{K}} = -85 \mu\text{V}\cdot\text{K}^{-1}$ (Figure 3b). S increases to $-120 \mu\text{V}\cdot\text{K}^{-1}$ at 800 K for both samples. $\rho_{300\text{K}} = 3\text{--}4 \text{ m}\Omega \text{ cm}$ and initially increases linearly and then saturates (Figure 3a) with a small residual resistivity of $\rho_{823\text{K}}/\rho_{323\text{K}} = 1.1\text{--}1.5$, typical of degenerate doping. The resulting S^2/ρ are $0.3\text{--}0.4 \text{ mW}\cdot\text{m}^{-1}\cdot\text{K}^{-2}$ at 800 K.

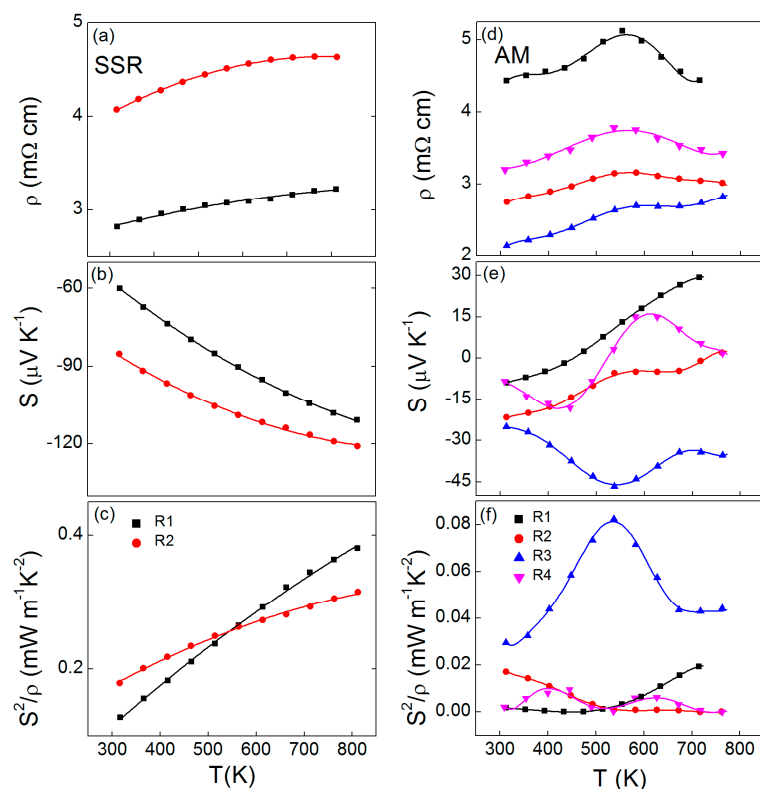


Figure 3. Temperature dependence of the electrical resistivity (ρ), Seebeck coefficient (S), and thermoelectric power factor (S^2/ρ) for (a–c) the powder route and (d–f) the arc-melted $\text{Ti}_{0.7}\text{V}_{0.3}\text{Co}_{0.85}\text{Fe}_{0.15}\text{Sb}_{0.7}\text{Sn}_{0.3}$ samples.

The AM samples have much smaller magnitudes of S and $R1$, $R2$ and $R4$ show n- to p-type transitions upon heating. All samples show a change in behaviour at $500\text{--}550 \text{ K}$, which corresponds closely to the melting point of elemental Sn (Figure 3e). For some samples, this leads to an S-wave

$S(T)$ shape, for others, the change appears as an inflection point. The magnitude of S remains small with values between -45 and $+30 \mu\text{V}\cdot\text{K}^{-1}$ in the $300\text{--}773 \text{ K}$ interval. $\rho_{300 \text{ K}} = 2\text{--}4.5 \text{ m}\Omega \text{ cm}$ is comparable to the SSR samples (Figure 3d). Due to the low S , the S^2/ρ for these samples remains small $<0.1 \text{ mW}\cdot\text{m}^{-1}\cdot\text{K}^{-2}$. The variations in $S(T)$ and $\rho(T)$ between AM samples are likely caused by small changes in HH composition, but do not track back to any clearly observable trend from XRD or SEM. The AM samples are balanced at the boundary between n- and p-type conduction, which is in keeping with the experimental HH composition, where the n-type doping due to V is compensated by Sn with no Fe present.

3.4. Thermal Conductivity and Figure of Merit

The temperature dependence of the total (κ) and lattice (κ_{lat}) thermal conductivities and the figures of merit for the SSR and AM samples are shown in Figure 4. $\kappa(T)$ is dominated by κ_{lat} and both show a $\sim 1/T$ temperature dependence. The magnitude of $\kappa_{\text{lat}, 323 \text{ K}}$ varies between $5\text{--}7 \text{ W}\cdot\text{m}^{-1}\cdot\text{K}^{-1}$ for the AM samples, while the SSR sample has slightly lower $\kappa_{\text{lat}, 323 \text{ K}} = 4.5 \text{ W}\cdot\text{m}^{-1}\cdot\text{K}^{-1}$. The large reduction compared to TiCoSb with $\kappa_{\text{lat}} = 18 \text{ W}\cdot\text{m}^{-1}\cdot\text{K}^{-1}$ at room temperature [37] is striking and must be related to microstructure effects. Phonon point-defect scattering can strongly reduce κ_{lat} , but this relies on mass differences and lattice strain caused by alloying [38]. The current substituents (V, Fe, and Sn) have similar masses and sizes to Ti, Co, and Sb. Even discounting their limited solubility, it is therefore difficult to see how the large κ_{lat} reduction can be explained by enhanced point-defect phonon scattering. Elemental Sn is a metallic conductor with a large κ and FH phases tend to be metallic with large κ values. The slightly larger κ_{lat} values for the AM samples are therefore consistent with the larger fractions of FH and Sn for those samples, but their presence cannot explain the overall low observed values. Similar strongly reduced κ_{lat} were observed in work on arc-melted $\text{Ti}_{0.9}\text{A}_{0.1}\text{CoSb}$ (A = Sc, V) samples and were attributed to interface effects [31]. The highest figure of merit, $ZT = 0.06$, is observed for the SSR sample that showed clear n-type behaviour. The small $S^2/\rho < 0.1 \text{ mW}\cdot\text{m}^{-1}\cdot\text{K}^{-2}$ for the AM samples, limits $ZT < 0.01$.

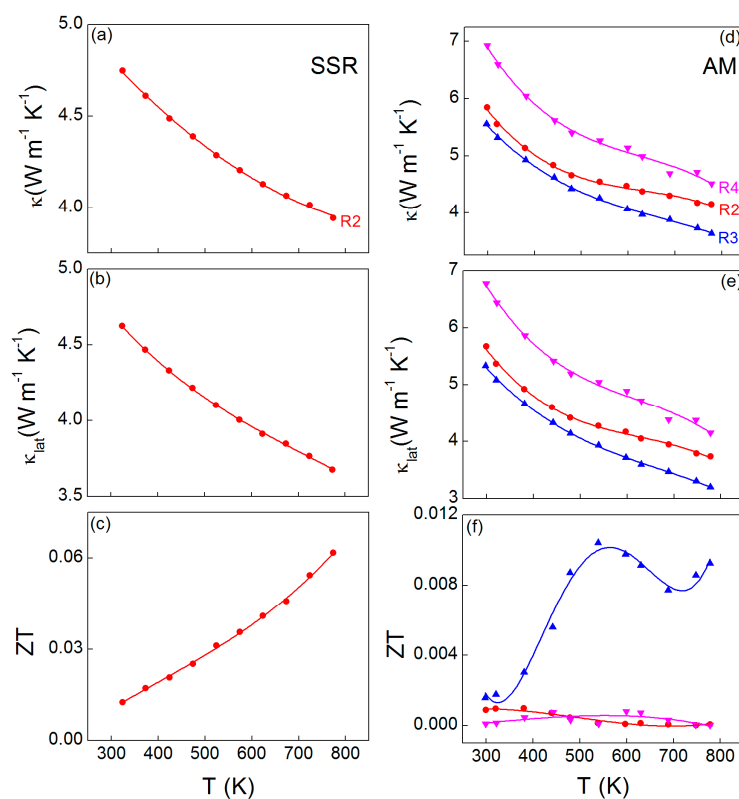


Figure 4. Temperature dependence of the total thermal conductivity (κ), the lattice thermal conductivity (κ_{lat}), and the thermoelectric figure of merit (ZT) for (a–c) the powder route and (d–f) the arc-melted $\text{Ti}_{0.7}\text{V}_{0.3}\text{Co}_{0.85}\text{Fe}_{0.15}\text{Sb}_{0.7}\text{Sn}_{0.3}$ samples.

4. Discussion

The aim of this work was to obtain a p-type TiCoSb-based HH alloy containing only abundant elements. Following on from previous work on the n-type $\text{Ti}_{1-x}\text{V}_x\text{CoSb}_{1-x}\text{Sn}_x$ HH alloys, Fe was substituted on the Co site to change the valence electron count to 17.85. Despite the good solubility of the individual elements and V and Sn in equimolar ratios, segregation of a competing $\text{V}(\text{Co}_{0.6}\text{Fe}_{0.4})_2\text{Sn}$ FH phase was observed in XRD and SEM. Samples prepared via arc melting showed a more complete segregation, leading to a complete absence of Fe, and ~ 0.1 V and ~ 0.1 Sn substitution in TiCoSb. The non-melt, powder route afforded more substitution with ~ 0.3 V, ~ 0.1 Fe, and ~ 0.1 Sn contained in the HH phase. From simple electron counting arguments, the AM samples are therefore expected to be near compensated, while the SSR samples should be n-type conductors. This is consistent with the experimental observations. Our work does not provide any evidence for the presence of competing HH phases. Calculations suggest miscibility gaps occur for substitutions on the X-site, leading to segregation into two HH phases [30,31]. This segregation is driven by destabilisation of the semiconducting electronic structure by changing the electron count. However, for the present samples, TiCoSb appears to avoid this destabilisation by instead segregating a $\text{V}(\text{Co}_{0.6}\text{Fe}_{0.4})_2\text{Sn}$ FH phase. Alternatively, the FH phase is the more stable phase, causing the HH phase to adjust its composition based on elements available. For the AM samples, this would occur by the FH crystallising first and leaving a melt with reduced V, Fe, and Sn content, leading to the formation of a HH poor in these elements. For the SSR samples, a similar product is found: A HH with reduced Fe and Sn content, but, interestingly, a near nominal amount of V. The ability to achieve a higher amount of V substitution must be a consequence of a different reaction pathway compared to the samples prepared via the melt. The observation of elemental Sn in the final product suggests that the ~ 0.1 Sn substitution onto the Sb-site that is found for both AM and SSR samples is an upper limit that is controlled by thermodynamics.

The microstructure of the AM samples reflects the higher stability of the FH phase. Upon cooling the FH crystallises first, followed by the HH and finally elemental Sn. This leads to the observed homogeneous microstructure of FH “islands”, surrounded by HH and Sn phases. By contrast, the SSR route does not proceed via the melt and a less uniform distribution of FH phases is observed, with a few larger areas and many rather small FH and Sn domains. Nevertheless, the composition of the FH and HH phases did not show much spatial variation, suggesting that the SSR samples have reached equilibrium under the sintering conditions. VFe_2Sn and VCo_2Sn are ferromagnetic metals with Curie temperatures of 200 and 70 K, respectively [39,40]. The $\text{V}(\text{Co}_{0.6}\text{Fe}_{0.4})_2\text{Sn}$ FH phase found in this work falls in between these end-members and our samples were not obviously ferromagnetic at room temperature.

The thermoelectric properties are consistent with the non-optimal doping and multiphase nature of the samples. The largest $S^2/\rho = 0.4 \text{ mW}\cdot\text{m}^{-1}\cdot\text{K}^{-2}$ is lower than the $\sim 2 \text{ mW}\cdot\text{m}^{-1}\cdot\text{K}^{-2}$ at 800 K that is possible for optimally doped p-type Fe substituted TiCoSb [29]. A final point of interest is the low $\kappa(T)$, which varies between $4.5\text{--}7 \text{ W}\cdot\text{m}^{-1}\cdot\text{K}^{-1}$ at 300 K, and is significantly reduced compared to pristine TiCoSb. Given the absence of significant point defect phonon scattering, this is likely related to the microstructure of these samples [31], which is characterised by the presence of multiple phases. A quantitative analysis of the impact of the interfaces between these different phases is beyond the scope of this manuscript. It is however, worth noting that the $\rho(T) \sim 2\text{--}4 \text{ m}\Omega \text{ cm}$ are not atypical for TiCoSb-based HHs (e.g., [26]) and this property therefore appears less affected than κ .

The results presented here demonstrate that stable FH phases can severely limit the amount of substitution in the HH phase. The most obvious way forward for further development of p-type TiCoSb-based materials is to reduce the number of substituents to two, e.g., the $\text{Ti}_{1-x}\text{V}_x\text{CoSb}_{1-z}\text{Sn}_z$ HHs with $z > x$. These compositions would hopefully continue to exhibit the improved high-temperature stability found previously [26]. The possible competing FH VCo_2Sn does not form up to $x \sim 0.4$ in the 18 electron $\text{Ti}_{1-x}\text{V}_x\text{CoSb}_{1-x}\text{Sn}_x$ series [26], suggesting that adjusting the V/Sn amounts is a viable route to achieve p-type conduction. Alternatively, removal of Sn would avoid any Sn-based FH phases, which appear more common than Sb-based FH phases containing Ti, V, Co, or Fe. It would therefore

be worthwhile exploring the $Ti_{1-x}V_xCo_{1-y}Fe_ySb$ compositions, where $y > x$ to achieve p-type electron counts.

To conclude, the simultaneous substitution of V, Fe, and Sn in TiCoSb is not possible for samples prepared using powder and arc-melting routes. This is due to the stability of a competing full-Heusler phase with $V(Co_{0.6}Fe_{0.4})_2Sn$ composition. This work extends knowledge on suitable p-type dopants and stability for the half-Heusler TiCoSb.

Author Contributions: M.A. and J.-W.G.B. conceived and designed the experiments; M.A. synthesised the samples and performed the structural and thermoelectric measurements; J.B. collected the SEM data; M.A. and J.-W.G.B. analysed the data; J.-W.G.B. wrote the paper with help of M.A.

Acknowledgments: M.A. acknowledges the British Council. J.-W.G.B. acknowledges the EPSRC for funding the research into half-Heuslers under grant number EP/N01717X/1. Raw data on which this publication is based can be accessed via the Heriot-Watt University Data Repository [41].

Conflicts of Interest: The authors declare no conflict of interest. The sponsors had no role in the design of the study; in the collection, analyses, or interpretation of data; in the writing of the manuscript, and in the decision to publish the results.

References

1. Bos, J.W.G.; Downie, R.A. Half-Heusler thermoelectrics: A complex class of materials. *J. Phys. Condens. Matter* **2014**, *26*, 433201.
2. Zhu, T.J.; Fu, C.G.; Xie, H.H.; Liu, Y.T.; Zhao, X.B. High Efficiency Half-Heusler Thermoelectric Materials for Energy Harvesting. *Adv. Energy Mater.* **2015**, *5*, 1500588.
3. Rowe, D.M. *Thermoelectrics and Its Energy Harvesting*; CRC Press: Boca Raton, FL, USA, 2012.
4. Schwall, M.; Balke, B. Phase separation as a key to a thermoelectric high efficiency. *Phys. Chem. Chem. Phys.* **2013**, *15*, 1868–1872.
5. Chen, L.; Gao, S.; Zeng, X.; Dehkordi, A.M.; Tritt, T.M.; Poon, S.J. Uncovering high thermoelectric figure of merit in (Hf,Zr)NiSn half-Heusler alloys. *Appl. Phys. Lett.* **2015**, *107*, 041902.
6. Gurth, M.; Rogl, G.; Romaka, V.V.; Grytsiv, A.; Bauer, E.; Rogl, P. Thermoelectric high ZT half-Heusler alloys $Ti_{1-x}Zr_xHf_yNiSn$ ($0 \leq x \leq 1$; $0 \leq y \leq 1$). *Acta Mater.* **2016**, *104*, 210–222.
7. Barczak, S.A.; Halpin, J.E.; Buckman, J.; Decourt, R.; Pollet, M.; Smith, R.I.; MacLaren, D.A.; Bos, J.W.G. Grain-by-Grain Compositional Variations and Interstitial Metals-A New Route toward Achieving High Performance in Half-Heusler Thermoelectrics. *ACS Appl. Mater. Interfaces* **2018**, *10*, 4786–4793.
8. Yan, X.A.; Joshi, G.; Liu, W.S.; Lan, Y.C.; Wang, H.; Lee, S.; Simonson, J.W.; Poon, S.J.; Tritt, T.M.; Chen, G.; et al. Enhanced Thermoelectric Figure of Merit of p-Type Half-Heuslers. *Nano Lett.* **2011**, *11*, 556–560.
9. Rausch, E.; Balke, B.; Ouardi, S.; Felser, C. Enhanced thermoelectric performance in the p-type half-Heusler (Ti/Zr/Hf)CoSb_{0.8}Sn_{0.2} system via phase separation. *Phys. Chem. Chem. Phys.* **2014**, *16*, 25258–25262.
10. Fu, C.G.; Bai, S.Q.; Liu, Y.T.; Tang, Y.S.; Chen, L.D.; Zhao, X.B.; Zhu, T.J. Realizing high figure of merit in heavy-band p-type half-Heusler thermoelectric materials. *Nat. Commun.* **2015**, *6*, 8144.
11. Fu, C.G.; Zhu, T.J.; Liu, Y.T.; Xie, H.H.; Zhao, X.B. Band engineering of high performance p-type FeNbSb based half-Heusler thermoelectric materials for figure of merit $zT > 1$. *Energy Environ. Sci.* **2015**, *8*, 216–220.
12. Hea, R.; Kraemer, D.; Mao, J.; Zeng, L.; Jie, Q.; Lan, Y.C.; Li, C.H.; Shuai, J.; Kim, H.S.; Liu, Y.; et al. Achieving high power factor and output power density in p-type half-Heuslers $Nb_{1-x}Ti_xFeSb$. *Proc. Natl. Acad. Sci. USA* **2016**, *113*, 13576–13581.
13. Xia, K.; Liu, Y.; Anand, S.; Snyder, G.J.; Xin, J.; Yu, J.; Zhao, X.; Zhu, T. Enhanced Thermoelectric Performance in 18-Electron Nb_{0.8}CoSb Half-Heusler Compound with Intrinsic Nb Vacancies. *Adv. Funct. Mater.* **2018**, *28*, 1705845.
14. Ferluccio, D.A.; Smith, R.I.; Buckman, J.; Bos, J.W.G. Impact of Nb vacancies and p-type doping of the NbCoSn-NbCoSb half-Heusler thermoelectrics. *Phys. Chem. Chem. Phys.* **2018**, *20*, 3979–3987.
15. Graf, T.; Felser, C.; Parkin, S.S.P. Simple rules for the understanding of Heusler compounds. *Prog. Solid State Chem.* **2011**, *39*, 1–50.
16. Downie, R.A.; MacLaren, D.A.; Smith, R.I.; Bos, J.W.G. Enhanced thermoelectric performance in TiNiSn-based half-Heuslers. *Chem. Commun.* **2013**, *49*, 4184–4186.

17. Birkel, C.S.; Douglas, J.E.; Lettiere, B.R.; Seward, G.; Verma, N.; Zhang, Y.C.; Pollock, T.M.; Seshadri, R.; Stucky, G.D. Improving the thermoelectric properties of half-Heusler TiNiSn through inclusion of a second full-Heusler phase: Microwave preparation and spark plasma sintering of TiNi_{1-x}Sn. *Phys. Chem. Chem. Phys.* **2013**, *15*, 6990–6997.
18. Chai, Y.W.; Kimura, Y. Microstructure evolution of nanoprecipitates in half-Heusler TiNiSn alloys. *Acta Mater.* **2013**, *61*, 6684–6697.
19. Douglas, J.E.; Birkel, C.S.; Verma, N.; Miller, V.M.; Miao, M.S.; Stucky, G.D.; Pollock, T.M.; Seshadri, R. Phase stability and property evolution of biphasic Ti-Ni-Sn alloys for use in thermoelectric applications. *J. Appl. Phys.* **2014**, *115*, 043720.
20. Downie, R.A.; Barczak, S.A.; Smith, R.I.; Bos, J.W.G. Compositions and thermoelectric properties of XNiSn (X = Ti, Zr, Hf) half-Heusler alloys. *J. Mater. Chem. C* **2015**, *3*, 10534–10542.
21. Downie, R.A.; Smith, R.I.; MacLaren, D.A.; Bos, J.W.G. Metal Distributions, Efficient n-Type Doping, and Evidence for in-Gap States in TiNiM_ySn (M = Co, Ni, Cu) half-Heusler Nanocomposites. *Chem. Mater.* **2015**, *27*, 2449–2459.
22. Berche, A.; Jund, P. Fully Ab-Initio Determination of the Thermoelectric Properties of Half-Heusler NiTiSn: Crucial Role of Interstitial Ni Defects. *Materials* **2018**, *11*, 868.
23. Dow, H.S.; Kim, W.S.; Shin, W.H. Effect of C and N Addition on Thermoelectric Properties of TiNiSn Half-Heusler Compounds. *Materials* **2018**, *11*, 262.
24. Levin, E.E.; Long, F.; Douglas, J.E.; Buffon, M.L.C.; Lamontagne, L.K.; Pollock, T.M.; Seshadri, R. Enhancing Thermoelectric Properties through Control of Nickel Interstitials and Phase Separation in Heusler/Half-Heusler TiNi_{1.1}Sn Composites. *Materials* **2018**, *11*, 903.
25. Schwall, M.; Balke, B. On the Phase Separation in n-Type Thermoelectric Half-Heusler Materials. *Materials* **2018**, *11*, 649.
26. Asaad, M.; Buckman, J.; Smith, R.I.; Bos, J.W.G. Thermoelectric properties and high-temperature stability of the Ti_{1-x}V_xCoSb_{1-x}Sn_x half-Heusler alloys. *RSC Adv.* **2016**, *6*, 56511–56517.
27. Tareuchi, N.; Goshō, K.; Hiroi, M.; Kawakami, M. The effect of V substitution on the properties of CoTiSb. *Phys. B Condens. Matter* **2005**, *359*, 1183–1185.
28. Sekimoto, T.; Kurosaki, K.; Muta, H.; Yamanaka, S. Thermoelectric properties of Sn-doped TiCoSb half-Heusler compounds. *J. Alloys Compd.* **2006**, *407*, 326–329.
29. Wu, T.; Jiang, W.; Li, X.; Zhou, Y.; Chen, L. Thermoelectric properties of p-type Fe-doped TiCoSb half-Heusler compounds. *J. Appl. Phys.* **2007**, *102*, 103705.
30. Mena, J.M.; Schoberth, H.G.; Gruhn, T.; Emmerich, H. Nanophase separation in CoSb-based half-Heusler thermoelectrics: A multiscale simulation study. *Phys Status Solidi A Appl. Mater. Sci.* **2016**, *213*, 706–715.
31. Mena, J.M.; Rausch, E.; Ouardi, S.; Gruhn, T.; Fecher, G.H.; Schoberth, H.G.; Emmerich, H.; Felser, C. Miscibility Gap in the Phase Diagrams of Thermoelectric Half-Heusler Materials CoTi_{1-x}Y_xSb (Y = Sc, V, Mn, Fe). *J. Electron. Mater.* **2016**, *45*, 1382–1388.
32. Larson, A.C.; von Dreele, R.B. *General Structure Analysis System (GSAS)*; Los Alamos National Laboratory Report LAUR 86-748; Los Alamos National Laboratory: Los Alamos, NM, USA, 2000.
33. Toby, B.H. EXPGUI, a graphical user interface for GSAS. *J. Appl. Crystallogr.* **2001**, 210–213.
34. Skovsen, I.; Bjerg, L.; Christensen, M.; Nishibori, E.; Balke, B.; Felser, C.; Iversen, B.B. Multi-temperature synchrotron PXRD and physical properties study of half-Heusler TiCoSb. *Dalton Trans.* **2010**, *39*, 10154–10159.
35. Kim, H.-S.; Gibbs, Z.M.; Tang, Y.; Wang, H.; Snyder, G.J. Characterization of Lorenz number with Seebeck coefficient measurement. *APL Mater.* **2015**, *3*, 041506.
36. Barczak, S.A.; Buckman, J.; Smith, R.I.; Baker, A.R.; Don, E.; Forbes, I.; Bos, J.W.G. Impact of Interstitial Ni on the Thermoelectric Properties of the Half-Heusler TiNiSn. *Materials* **2018**, *11*, 536.
37. Zhou, M.; Chen, L.D.; Zhang, W.Q.; Feng, C.D. Disorder scattering effect on the high-temperature lattice thermal conductivity of TiCoSb-based half-Heusler compounds. *J. Appl. Phys.* **2005**, *98*, 013708.
38. Yang, J.; Meisner, G.P.; Chen, L. Strain field fluctuation effects on lattice thermal conductivity of ZrNiSn-based thermoelectric compounds. *Appl. Phys. Lett.* **2004**, *85*, 1140–1142.
39. Kübler, J.; Fecher, G.H.; Felser, C. Understanding the trend in the Curie temperatures of Co₂-based Heusler compounds: Ab initio calculations. *Phys. Rev. B* **2007**, *76*, 024414.

40. Vanengen, P.G.; Buschow, K.H.J.; Erman, M. Magnetic-properties and magneto-optical spectroscopy of heusler alloys based on transition metals and Sn. *J. Magn. Magn. Mater.* **1983**, *30*, 374–382.
41. Data Underpinning. Available online: <https://doi.org/10.17861/e6cdebd6-56ec-4606-881a-7eb3c4f12050> (accessed on 12 November 2018).



© 2018 by the authors. Licensee MDPI, Basel, Switzerland. This article is an open access article distributed under the terms and conditions of the Creative Commons Attribution (CC BY) license (<http://creativecommons.org/licenses/by/4.0/>).